Quasiparticle interference of Fermi arc states in the type-II Weyl semimetal candidate WTe_2

Yuan Yuan,[1] Xing Yang,[1] Lang Peng,[1] Zhi-Jun Wang,[2] Jian Li,[3] Chang-Jiang Yi,[4] Jing-Jing Xian,[1]
You-Guo Shi,[4] and Ying-Shuang Fu[1,*]
[1]*School of Physics and Wuhan National High Magnetic Field Center, Huazhong University of Science and Technology, Wuhan 430074, China*
[2]*Department of Physics, Princeton University, New Jersey 08544, USA*
[3]*Westlake University, Hangzhou, Zhejiang Province, China*
[4]*Institute of Physics, Chinese Academy of Sciences, Beijing 100084, China*

(Received 15 January 2018; published 26 April 2018)

Weyl semimetals possess linear dispersions through pairs of Weyl nodes in three-dimensional momentum spaces, whose hallmark arclike surface states are connected to Weyl nodes with different chirality. WTe_2 was recently predicted to be a new type of Weyl semimetal. Here, we study the quasiparticle interference (QPI) of its Fermi arc surface states by combined spectroscopic-imaging scanning tunneling spectroscopy and density functional theory calculations. We observed the electron scattering on two types of WTe_2 surfaces unambiguously. Its scattering signal can be ascribed mainly to trivial surface states. We also address the QPI feature of nontrivial surface states from theoretical calculations. The experimental QPI patterns show some features that are likely related to the nontrivial Fermi arc states, whose existence is, however, not conclusive. Our study provides an indispensable clue for studying the Weyl semimetal phase in WTe_2.

DOI: 10.1103/PhysRevB.97.165435

I. INTRODUCTION

Weyl fermions are massless chiral particles that possess nondegenerate linear energy dispersions through nodes, i.e., Weyl nodes, in three dimensions (3D) [1]. The Weyl nodes always appear in pairs with opposite chirality and can be robust against perturbations unless they are annihilated by each other. Despite their original prediction in particle physics, their existence as low-energy excitations in the energy bands of crystalline solids named as Weyl semimetals has drawn extensive attention [2,3], because they provide a novel platform for examining the relativistic quantum phenomena such as chiral anomaly transport [4,5]. Depending on the shape of the bulk Fermi surface, the Weyl semimetals are classified into two categories. In type-I Weyl semimetals, conduction and valence pockets have energy overlap solely at Weyl nodes, whose bulk Fermi surface is thus pointlike as exemplified in TaAs families [6]. Type-II Weyl semimetals predicted in WTe_2 class materials have Weyl nodes appearing at touching points of energetically overlapped conduction and valence bands, whose Fermi surface has finite density of states [7–10]. Unlike the type-I Weyl semimetals, the type-II Weyl semimetals break the Lorentz symmetry and have no analogous particles in nature.

Weyl semimetals can be considered as a series of strongly coupled stacks of two-dimensional (2D) quantum anomalous Hall insulators. As a result, the nontrivial bulk bands of Weyl semimetals projected onto the surface generate nonclosed topological Fermi arc surface states, which in turn act as a fingerprint of the Weyl semimetal phase [11,12]. With angle-resolved photoemission spectroscopy (ARPES), the topological Fermi arc states have been successfully observed in the type-I Weyl semimetal TaAs [13,14] and TaP [15], as well as the type-II Weyl semimetal $MoTe_2$ [16–18].

Although WTe_2 is the first predicted type-II Weyl semimetal, its topological Fermi arc states are more difficult to probe and still lack experimental proof. For one thing, the momentum separation of its Weyl points constitutes only ~0.7% of the Brillouin zone on the (001) surface, making the size of its topological Fermi arc states extremely small [7]. For another, they are located above the Fermi level [7]. Although its trivial Fermi arc states with large wave vectors have been observed with ARPES [19–23], the small topological arcs have not been resolved. In principle, quasiparticle interference (QPI) based on spectroscopic-imaging scanning tunneling microscopy (SISTM) can get access to both occupied and unoccupied energy states with high-energy resolution, which is suitable for the current study. The STM QPI technique has shown success in identifying the topological surface states of topological insulators [24,25] and the topological Fermi arc states of Weyl semimetal TaAs [26,27], NbP [28], $MoTe_2$ [16,29], and $Mo_{0.66}W_{0.34}Te_2$ [30].

The WTe_2 crystal has $1T'$ structure, that is layer stacked along its [001] direction [Fig. 1(a)]. Each layer is composed of a W atom layer sandwiched between two Te atom layers, where the W atoms are laterally distorted towards the *b* direction of the otherwise $1T$ structure, forming Te chains of alternating heights along the *a* direction. Due to the lack of inversion symmetry in WTe_2, the two Te surfaces at both sides of the W atomic plane are inequivalent, and are named as "top surface" and "bottom surface," respectively [Fig. 1(a)]. Although the two surfaces are identical in their top view, they are distinguished from the relative heights between the W atomic planes and the

---

[*] yfu@hust.edu.cn

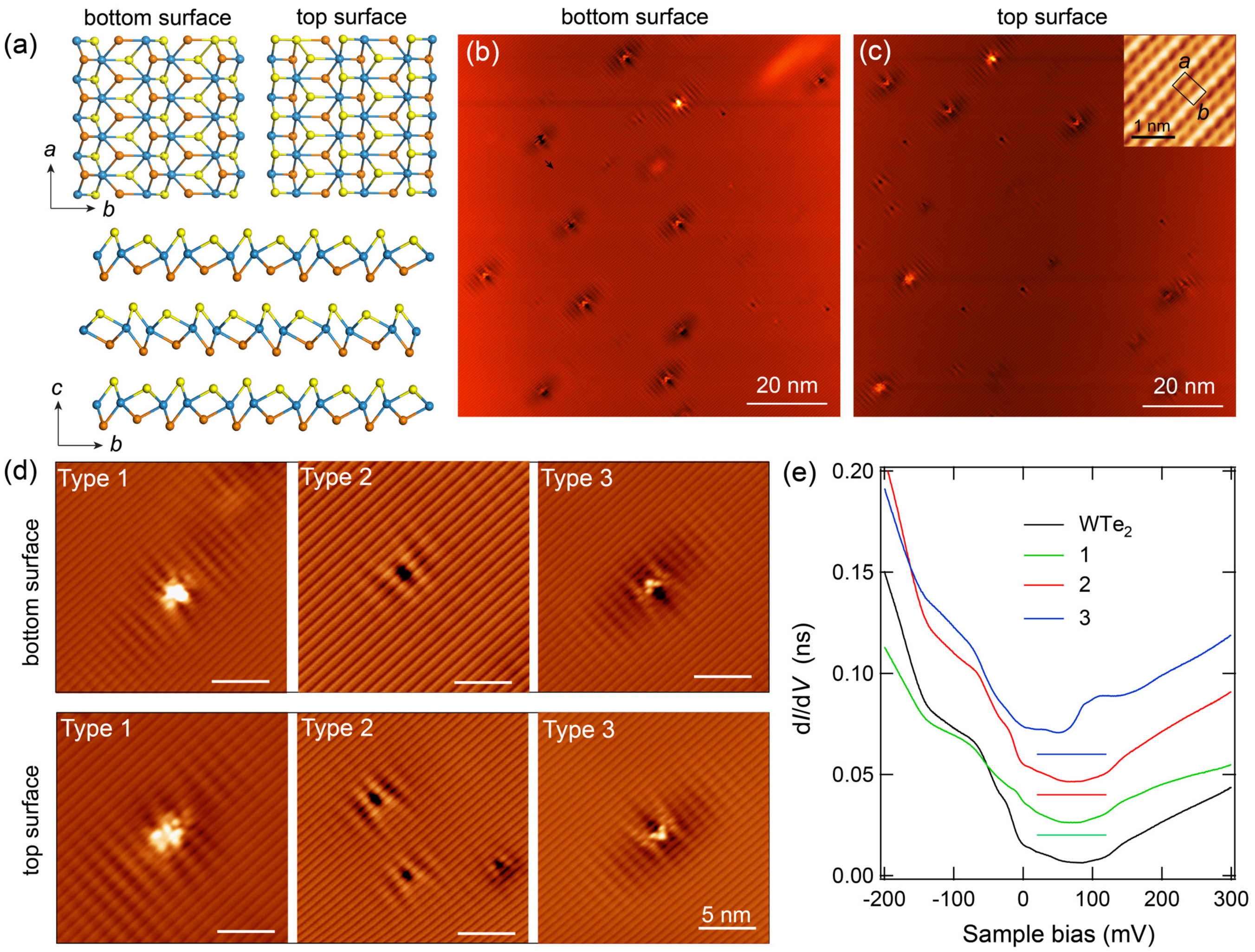

FIG. 1. Sample morphology and defect states. (a) Top view (top) and side view (bottom) of the crystal structure of $1T'$-WTe$_2$, showing two types of surfaces. The W atoms, the Te atoms of the top surfaces, and the Te atoms of the bottom surfaces are depicted with blue, yellow, and orange balls, respectively. (b),(c) STM topography of the bottom (b) and top (c) surfaces of WTe$_2$. A high-resolution STM image shows the atomic resolution of WTe$_2$, whose unit cell is marked with a black rectangle [inset of (c)]. (d) Magnified view of the three types of defects observed on the top and bottom surface, respectively. The scale bar for all images in (c),(d) is 5 nm. (e) Tunneling spectra of the three types of defects and bare WTe$_2$ surface. The spectra have been shifted by 0.02 nS for each curve, whose zero conductance values have been marked with horizontal line segments. Imaging conditions: $V_s = 30\,\text{mV}$, $I_t = 100\,\text{pA}$ for (b),(c); $V_s = 120\,\text{mV}$, $I_t = 100\,\text{pA}$ for [(b), inset]; $V_s = 30\,\text{mV}$, $I_t = 100\,\text{pA}$ for (d).

average Te planes of the two surfaces [19]. Previous theoretical study predicts that the two surfaces possess different surface state characteristics as a result of the inversion symmetry breaking [7]. There exist trivial Fermi arc surface states with large wave vectors on both types of surfaces, which differ in their detailed band dispersions. Notably, the topological Fermi arc states are predicted to be prominent solely on the bottom surface and barely distinguishable on the top surface (see the Supplemental Material [31]). To this end, it is highly desirable to study the QPI of both surfaces in an unambiguous manner. Albeit very recently two QPI studies on WTe$_2$ surfaces have been performed [32,33], clear signatures distinguishing the two surfaces are yet to be observed.

Here, we performed STM-based QPI on WTe$_2$ in combination with density functional theory (DFT) calculations aiming to identify the QPI feature of topological Fermi arc states. We achieved the measuring of QPI from native defects on both top and bottom surfaces, which can be ascribed to scattering mainly from trivial surface states. We also address the QPI feature of nontrivial surface states from DFT calculations, whose experimental detection is, however, not conclusive.

II. EXPERIMENT

The experiments were performed with a custom-made Unisoku STM (1300) at 4.4 K [34]. WTe$_2$ crystals grown by a solid-state reaction were cleaved *in situ* under ultrahigh-vacuum conditions at ~77 K. After cleaving, the crystals were transferred quickly to low-temperature STM for subsequent measurements. The tunneling spectra were obtained by lock-in detection of the tunneling current with a modulation voltage of 3.54 mV$_{\text{rms}}$ at 983 Hz feeding into the sample bias. The electronic structure calculations were based on DFT as

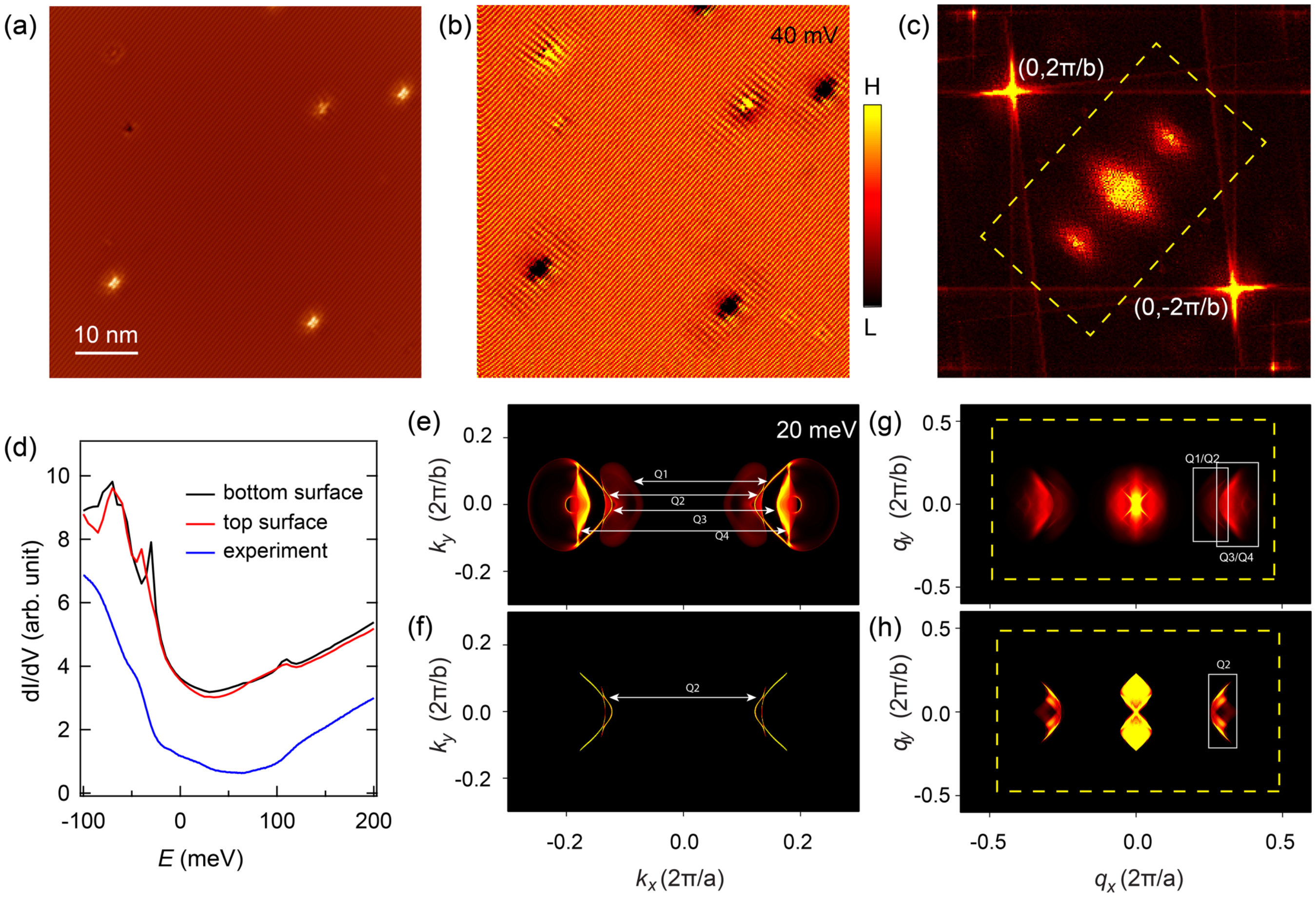

FIG. 2. Experimental QPI of $\mathrm{WTe_2}$ at 40 mV and its DFT simulation. (a),(b) Topography of the bottom surface $\mathrm{WTe_2}$ (a) and its dI/dV conductance map at 40 mV (b). Imaging conditions for (a): $V_s = 300$ mV, $I_t = 50$ pA. Set point conditions for (b): $V_s = 180$ mV, $I_t = 600$ pA. (c) Symmetrized FFT of the dI/dV map in (b). (d) Calculated (black and red curves) and measured (blue curve) dI/dV spectra of the two surfaces. (e),(g) Calculated SWCEC at 20 meV of the bottom surface and its corresponding SSP map. (f),(h) CECs of the trivial surface arc states extracted from (e) and its corresponding SSP map (h). The yellow rectangles in (c),(g),(h) mark the same size of the q space. The interpocket scattering configurations are marked in (e)–(h).

implemented in the Vienna *ab initio* simulation package [35], and used the core-electron projector augmented wave basis sets [36] with the generalized-gradient method [37]. Spin-orbital coupling was included self-consistently. The cutoff energy for wave-function expansion was 300 eV. Experimental lattice parameters were used throughout our calculations. The spin-dependent scattering probability (SSP) was subsequently calculated from the spectral density and the spin density obtained from DFT calculations [38].

A high-resolution STM image of a cleaved $\mathrm{WTe_2}$ (001) surface clearly resolves the atomic chains of Te atoms, whose unit cell is measured as $a = 3.45$ Å, $b = 6.12$ Å and is consistent with its crystal structure [Fig. 1(c), inset]. Figures 1(b) and 1(c) display two large-scale topographic images of two areas of the same sample, showing atomic defects. Scrutiny of the symmetry of the defects indicates the two areas may belong to different domains. There are typically three kinds of native defects generated during the crystal growth [Fig. 1(d)]. They all have mirror symmetry relative to the b direction. Evidently, the same kinds of defects are mirror symmetric relative to the a direction, which implies the two areas are likely of two different surfaces, i.e., top and bottom surfaces. In the following, we show that is indeed the case with our QPI measurements in conjunction with DFT calculations.

The defects exhibit distinct spectroscopic features [Fig. 1(e)]. While the type-1 and type-2 defects only show minute conductance modifications compared to that of the clean $\mathrm{WTe_2}$ surface, the type-3 defect features a prominent conductance peak centered around 100 meV with a width of ∼50 meV. Despite the origins of the defects currently being unknown, they all serve as scattering centers for QPI mapping. For that purpose, we first selected an area with densely populated defects on the bottom surface and measured its conductance mappings at different energies [Fig. 2(a)]. Figure 2(b) gives an example at 40 mV with an image size of 60 nm. Ripplelike patterns are clearly resolved in the vicinity of the defects that are elongated along the chain direction [39] and disperse with imaging energy, demonstrating they are standing waves that originate from the scattering of highly anisotropic band dispersions of $\mathrm{WTe_2}$. To deliver information in the reciprocal space, we performed fast Fourier transformation (FFT) to the real-space QPI mapping, which was twofold symmetrized to enhance its signal-to-noise ratio [Fig. 2(c)]. There are two bright dots residing at the top-left and bottom-right corners of the FFT pattern whose locations stay the same at different energies. They are the Bragg points of $[0,\pm(2\pi/b)]$, which correspond to the atomic lattice of the b direction. The main body of the QPI map marked in the yellow rectangle consists of one elliptical-shaped pocket in the center and two crescent-shaped patterns symmetrically located on the q_x direction.

To interpret the QPI pattern, we calculated the surface-weighted constant energy contours (SWCECs) of the bottom surface and the corresponding scattering probability maps by DFT. The calculated density of states (DOS) spectra can be obtained by summing up the SWCECs at different energies. There is a slight difference in the calculated DOS spectra of the two surfaces, because of their different surface states [Fig. 2(d)]. However, such a subtle difference is barely distinguished in the experimental dI/dV spectra. After shifting the calculated spectra to higher energy by 20 meV, an excellent match with the experiment is obtained [Fig. 2(d)]. Therefore, the energetically shifted scattering probability maps were compared with the QPI pattern. Since the bulk states and the surface states are all spin polarized in momentum space [22], their scattering probability should be spin dependent [24]. Figure 2(e) shows the calculated SWCEC at 20 meV, which features hole pockets and electron pockets symmetrically located at the inner and outer Brillouin zone along the k_x direction, respectively. There is a trivial Fermi arc surface state traversing through the hole pocket and connecting back to the electron pocket, whose CEC is selectively plotted in Fig. 2(f). Figures 2(g) and 2(h) are the calculated spin-dependent scattering probability map (SSP) of the SWCECs of the whole states and the trivial surface state, respectively. Evidently, the SSP of the surface state has better agreement with the measured QPI pattern, demonstrating the dominant contribution of the surface state to the scattering signals. This phenomenon can be rationalized from two aspects. For one thing, the surface state is easily detectable to the tunneling current due to its large weight at the surface. For another, the surface state is confined to two dimensions, where coherent standing waves can form more readily than the bulk states whose scatterings are allowed in all directions [16,30].

Based on the above comparison, we calculated the energy-dependent SWCECs and SSP mappings to unveil the evolution of the experimental QPI patterns. Figure 3 shows the CECs of the whole states [Figs. 3(a)–3(d)], selected surface states [Figs. 3(e)–3(h)] and their corresponding SSP mappings [Figs. 3(i)–3(p)], together with the experimental QPI [Figs. 3(q)–3(t)] at four representative energies. More SWCECs and QPI mappings are displayed in the Supplemental Material [31]. The SSP mappings of the surface state can quantitatively reproduce the experimental QPI patterns at the finite q vectors with the crescent shapes that are marked with white rectangles in Figs. 3(m)–3(t). Further, the detailed energy evolution of the crescent feature, which is extracted by doing a line cut along the q_x direction of the QPI map [Figs. 3(v) and 3(w)], also agrees well with that of the theoretical calculation [Fig. 3(u)]. This indicates the trivial Fermi arc states are clearly manifested from the QPI patterns. A large crescent-shaped feature is seen in the QPI pattern of 0 meV [marked with a green arrow in Fig. 3(q)], which corresponds to a scattering vector between the surface state and the bulk state. This demonstrates the bulk states also get involved in the QPI scattering at certain energies. At the theoretical SSP mappings of all the four energies, there exists an X-shaped feature around the zero q vector, which was attributed as a characteristic scattering from the trivial Fermi arc states in Ref. [38]. However, such a feature was not resolved in our experiment. We rationalize such discrepancy by considering the fact that the zero q vectors are sensitive to extrinsic long-range features in our conductance maps, which may superimpose with the X-shaped feature. Rather, the large crescent feature at finite q vectors is proven more reliable to detect the scattering from the surface Fermi arc states.

In addition to the trivial surface state, we scrutinize the scattering feature of the nontrivial surface state. As is shown in the CECs of 70 meV in Fig. 3(g), the nontrivial Fermi arc surface states appear as four small spots due to their tiny sections connecting to the four pairs of Weyl points. Such small arcs can hardly be resolved with ARPES even if they were in occupied states. However, the nontrivial arc states can be amplified via their scattering with the trivial Fermi arc states, which provides an opportunity to detect them in the QPI experiment. We have theoretically explored this possibility in the calculated SSP maps. Figure 3(o) shows the nontrivial Fermi arc states are manifested as a cross superimposed on the crescent-shaped SSP mapping of the trivial arc states. Although the experimental QPI pattern indeed exhibits a crosslike feature at the expected q vectors [Fig. 3(s)], the signal is not strong enough to draw a conclusive statement.

A similar analysis scheme is applied to the top surface (Fig. 4) (Supplemental Material [31]). By comparing both the calculated SSP maps ([Figs. 4(i)–4(p)] of the CECs [Figs. 4(a)–4(h)] and their corresponding energy dispersion relation [Fig. 4(u)] with those of the experimental QPI patterns [Figs. 4(q)–4(t), 4(v), and 4(w)], we conclude that the trivial Fermi arc surface states dominantly contribute to the QPI scattering signals, which is similar to the case of the bottom surface. The large crescent-shaped feature coming from the scattering of bulk states is also observed [Fig. 4(q)]. More importantly, comparison between Figs. 3(a)–3(h) and 4(a)–4(h) shows the detailed shapes of the CECs between the two surfaces are different, as is particularly highlighted in the CECs at −20 meV [Figs. 3(e) and 4(e)]. Interestingly, such difference is also identified in the QPI pattern [Figs. 3(q) and 4(q)]. It is noted that our observation is distinct from a previous study, where the two surfaces were obtained by flipping the crystal before cleaving but no difference in the QPI pattern of the two surfaces was observed [32]. We argue the discrepancy may come from the invalid assumption of the single-domain state in WTe_2. As is indicated from a spot focused ARPES study, the crystal is not in a single-domain state, where the two surfaces coexist at different domains [19]. Thus, flipping the crystal does not guarantee the obtainment of the different surface. Notably, unlike its bottom surface counterpart, a crosslike scattering feature is not seen in the QPI pattern at 90 meV [Fig. 4(s)]. This is in agreement with the SSP map at 70 meV, where the topological arc state at the top surface is indistinguishable and makes no contribution to the scattering signal [Fig. 4(o)].

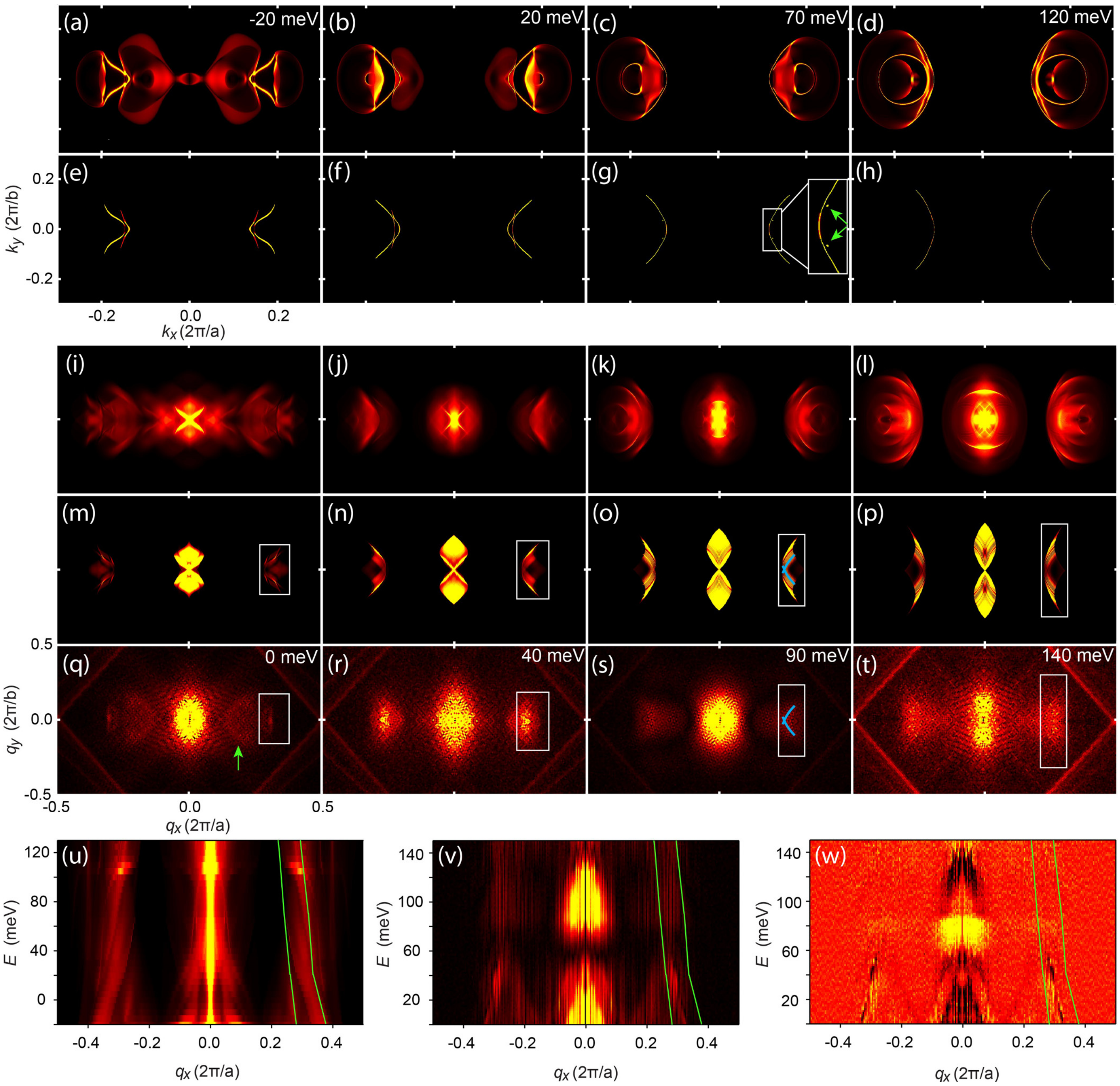

FIG. 3. Comparison between QPI patterns and SSP maps of bottom surface at various energies. (a)–(d) Calculated SWCECs of the bottom surface at −20, 20, 70, and 120 meV. (e–h) CECs of the surface states extracted from (a)–(d). The topological arcs are seen as two dots (indicated with green arrows) adjacent to the large trivial arc in the magnified view of the rectangle in (g). (i)–(l) SSP maps of the SWCEC in (a)–(d). (m)–(p) SSP maps of the CEC of (e)–(h). (q)–(t) QPI patterns measured at 0, 40, 90, and 140 mV. The rectangle areas in (m)–(t) mark the comparison between the SSP maps and the experimental QPI patterns. A green arrow in (q) marks the scattering between surface states and bulk states. The scattering pattern between topological arcs and the trivial arcs is marked as a blue cross in (o) and (s). (u),(v) Energy dispersion along the q_x direction extracted from the SSP map of the SWCECs (u) and from the QPI pattern (v), respectively. (w) Derivative image of (v). The green lines in (u)–(w) mark the range of the q_x vectors associated to interarc scattering, which are extracted from the SSP maps of the trivial surface state. Set point conditions for (q)–(t): $V_s = 180\,\text{mV}$, $I_t = 600\,\text{pA}$.

III. DISCUSSION

Our work imposes several implications for future studies of similar systems. First, the electronic structure of WTe_2 is complicated with multiple bulk pockets and trivial as well as topological Fermi arc surface states. This makes the interpretation of QPI patterns challenging. Our study, in conjunction with several other studies [29,30,32,33], indicates that the surface states dominantly contribute to the scattering signals, which signifies the convenient filtering of complicated bulk states in QPI experiments and is of significance for studying other similar systems. Second, unlike previous QPI studies focusing only on the topological arc states of $MoTe_2$ [16,29], our study

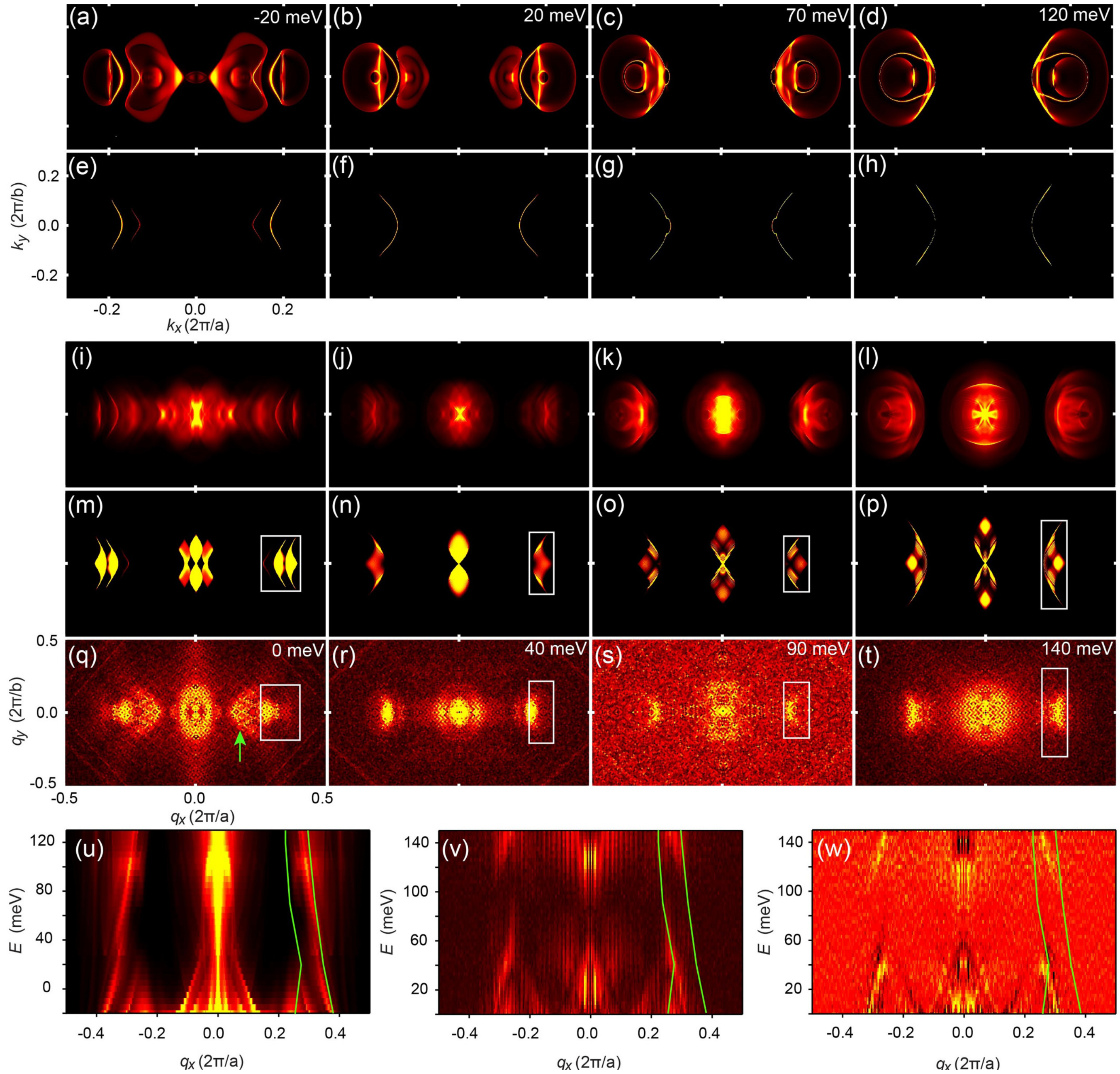

FIG. 4. Comparison between QPI patterns and SSP maps of top surface at various energies. (a)–(d) Calculated SWCECs of the top surface at −20, 20, 70, and 120 meV. (e)–(h) CECs of the trivial surface states extracted from (a)–(d). (i)–(l) SSP maps of the SWCECs in (a)–(d). (m)–(p) SSP maps of the CECs of (e)–(h). (q)–(t) QPI patterns measured at 0, 40, 90, and 140 mV. The rectangle areas in (m)–(t) mark the comparison between the SSP maps and the experimental QPI patterns. A green arrow in (q) marks the scattering between trivial surface states and bulk states. (u),(v) Energy dispersion along the q_x direction extracted from the SSP map of the SWCECs (u) and from the QPI pattern (v), respectively. (w) Derivative image of (v). The green lines in (u)–(w) mark the range of the q_x vectors associated to interarc scattering, which are extracted from the SSP maps of the trivial surface state. Set point conditions for (q)–(t): $V_s = 150\,\mathrm{mV}$, $I_t = 430\,\mathrm{pA}$.

indicates the trivial and topological arc surface states should be treated on an equal footing. Third, Weyl semimetals that lack inversion symmetry have different electronic characteristics in their surface states on the top and bottom surfaces. It is essential to study both surfaces, especially when the topological arc states are distinguished only on one surface as is exemplified in WTe_2.

IV. SUMMARY

In conclusion, we have investigated the QPI of $1T'$-WTe_2 at its two different surfaces. Both experimental SI-STM measurements and theoretical DFT calculations jointly reveal the dominate scattering from the trivial surface arc states. A hallmark signature of the topological Fermi arc scattering is theoretically proposed and experimentally detected, whose signal is, however, insufficient to draw a conclusive statement. Our work paves the way for further investigations towards the topological surface arc states.

ACKNOWLEDGMENTS

We thank Z.W. Zhu, X. Dai, G. Li, and T. Hanaguri for helpful discussion. This work is funded by the National Key Research and Development Program of China (Grants No. 2017YFA0403501 and No. 2016YFA0401003), the National Science Foundation of China (Grants No. 11474112, No. 11522431, No. 11774399, No. 11474330, and No. 11504117), and the Chinese Academy of Sciences (Grants No. XDB07020100 and No. QYZDB-SSW-SLH043).

---

[1] H. Weyl, Z. Phys. **56**, 330 (1929).

[2] X. Wan, A. M. Turner, A. Vishwanath, and S. Y. Savrasov, Phys. Rev. B **83**, 205101 (2011).

[3] G. Xu, H. Weng, Z. Wang, X. Dai, and Z. Fang, Phys. Rev. Lett. **107**, 186806 (2011).

[4] H. B. Nielsen and M. Ninomiya, Phys. Lett. B **130**, 389 (1983).

[5] A. A. Zyuzin and A. A. Burkov, Phys. Rev. B **86**, 115133 (2012).

[6] H. Weng, C. Fang, Z. Fang, B. A. Bernevig, and X. Dai, Phys. Rev. X **5**, 011029 (2015).

[7] A. A. Soluyanov, D. Gresch, Z. J. Wang, Q. S. Wu, M. Troyer, X. Dai, and B. A. Bernevig, Nature **527**, 495 (2015).

[8] Y. Xu, F. Zhang, and C. Zhang, Phys. Rev. Lett. **115**, 265304 (2015).

[9] Y. Sun, S. C. Wu, M. N. Ali, C. Felser, and B. Yan, Phys. Rev. B **92**, 161107 (2015).

[10] T. R. Chang, S. Y. Xu, G. Q. Chang, C. C. Lee, S. M. Huang, B. K. Wang, G. Bian, H. Zheng, D. S. Sanchez, I. Belopolski, N. Alidoust, M. Neupane, A. Bansil, H. T. Jeng, H. Lin, and M. Z. Hasan, Nat. Commun. **7**, 10639 (2016).

[11] M. Z. Hasan, S. Y. Xu, I. Belopolski, and S. M. Huang, Annu. Rev. Condens. Matter Phys. **8**, 289 (2017).

[12] B. Yan and C. Felser, Annu. Rev. Condens. Matter Phys. **8**, 1 (2017).

[13] S. Y. Xu, I. Belopolski, N. Alidoust, M. Neupane, G. Bian, C. L. Zhang, R. Sankar, G. Q. Chang, Z. J. Yuan, C. C. Lee, S. M. Huang, H. Zheng, J. Ma, D. S. Sanchez, B. K. Wang, A. Bansil, F. C. Chou, P. P. Shibayev, H. Lin, S. Jia *et al.*, Science **349**, 613 (2015).

[14] B. Q. Lv, H. M. Weng, B. B. Fu, X. P. Wang, H. Miao, J. Ma, P. Richard, X. C. Huang, L. X. Zhao, G. F. Chen, Z. Fang, X. Dai, T. Qian, and H. Ding, Phys. Rev. X **5**, 031013 (2015).

[15] B. Q. Lv, N. Xu, H. M. Weng, J. Z. Ma, P. Richard, X. C. Huang, L.X. Zhao, G. F. Chen, C. E. Matt, F. Bisti, V. N. Strocov, J. Mesot, Z. Fang, X. Dai, T. Qian, M. Shi, and H. Ding, Nat. Phys. **11**, 724 (2015).

[16] K. Deng, G. L. Wan, P. Deng, K. N. Zhang, S. J. Ding, E. Wang, M. Z. Yan, H. Q. Huang, H. Y. Zhang, Z. L. Xu, J. Denlinger, A. Fedorov, H. T. Yang, W. H. Duan, H. Yao, Y. Wu, S. S. Fan, H. J. Zhang, X. Chen, and S. Y. Zhou, Nat. Phys. **12**, 1105 (2016).

[17] L. N. Huang, T. M. McCormick, M. Ochi, Z. Y. Zhao, M. T. Suzuki, R. Arita, Y. Wu, D. X. Mou, H. B. Cao, J. Q. Yan, N. Trivedi, and A. Kaminski, Nat. Mater. **15**, 1155 (2016).

[18] J. Jiang, Z. K. Liu, Y. Sun, H. F. Yang, C. R. Rajamathi, Y. P. Qi, L. X. Yang, C. Chen, H. Peng, C. C. Hwang, S. Z. Sun, S. K. Mo, I. Vobornik, J. Fujii, S. S. P. Parkin, C. Felser, B. H. Yan, and Y. L. Chen, Nat. Commun. **8**, 13973 (2017).

[19] F. Y. Bruno, A. Tamai, Q. S. Wu, I. Cucchi, C. Barreteau, A. de la Torre, S. McKeown Walker, S. Riccò, Z. Wang, T. K. Kim, M. Hoesch, M. Shi, N. C. Plumb, E. Giannini, A. A. Soluyanov, and F. Baumberger, Phys. Rev. B **94**, 121112(R) (2016).

[20] Y. Wu, D. X. Mou, N. H. Jo, K. W. Sun, L. N. Huang, S. L. Bud'ko, P. C. Canfield, and A. Kaminski, Phys. Rev. B **94**, 121113(R) (2016).

[21] J. Sánchez-Barriga, M. G. Vergniory, D. Evtushinsky, I. Aguilera, A. Varykhalov, S. Blügel, and O. Rader, Phys. Rev. B **94**, 161401(R) (2016).

[22] B. J. Feng, Y. H. Chan, Y. Feng, R. Y. Liu, M. Y. Chou, K. Kuroda, K. Yaji, A. Harasawa, P. Moras, A. Barinov, W. Malaeb, C. Bareille, T. Kondo, S. Shin, F. Komori, T. C. Chiang, Y. G. Shi, and I. Matsuda, Phys. Rev. B **94**, 195134 (2016).

[23] C. L. Wang, Y. Zhang, J. W. Huang, S. Nie, G. D. Liu, A. J. Liang, Y. X. Zhang, B. Shen, J. Liu, C. Hu, Y. Ding, D. F. Liu, Y. Hu, S. L. He, L. Zhao, L. Yu, J. Hu, J. Wei, Z. Q. Mao, Y. G. Shi *et al.*, Phys. Rev. B **94**, 241119(R) (2016).

[24] P. Roushan, J. Seo, C. V. Parker, Y. S. Hor, D. Hsieh, D. Qian, A. Richardella, M. Z. Hasan, R. J. Cava, and A. Yazdani, Nature **460**, 1106 (2009).

[25] T. Zhang, P. Cheng, X. Chen, J. F. Jia, X. C. Ma, K. He, L. L. Wang, H. J. Zhang, X. Dai, Z. Fang, X. C. Xie, and Q. K. Xue, Phys. Rev. Lett. **103**, 266803 (2009).

[26] H. Inoue, A. Gyenis, Z. Wang, J. Li, S. W. Oh, S. Jiang, N. Ni, B. A. Bernevig, and A. Yazdani, Science **351**, 1184 (2016).

[27] R. Batabyal, N. Morali, N. Avraham, Y. Sun, M. Schmidt, C. Felser, A. Stern, B. Yan, and H. Beidenkopf, Sci. Adv. **2**, e1600709 (2016).

[28] H. Zheng, S. Y. Xu, G. Bian, C. Guo, G. Q. Chang, D. S. Sanchez, I. Belopolski, C. C. Lee, S. M. Huang, X. Zhang, R. Sankar, N. Alidoust, T. R. Chang, F. Wu, T. Neupert, F. C. Chou, H. T. Jeng, N. Yao, A. Bansil, S. Jia *et al.*, ACS Nano **10**, 1378 (2016).

[29] P. Deng, Z. L. Xu, K. Deng, K. N. Zhang, Y. Wu, H. J. Zhang, S. Y. Zhou, and X. Chen, Phys. Rev. B **95**, 245110 (2017).

[30] H. Zheng, G. Bian, G. Q. Chang, H. Lu, S. Y. Xu, G. Q. Wang, T. R. Chang, S. T. Zhang, I. Belopolski, N. Alidoust, D. S. Sanchez, F. Q. Song, H. T. Jeng, N. Yao, A. Bansil, S. Jia, H. Lin, and M. Z. Hasan, Phys. Rev. Lett. **117**, 266804 (2016).

[31] See Supplemental Material at http://link.aps.org/supplemental/10.1103/PhysRevB.97.165435 for the calculated topological Fermi arc surface states, the surface-weighted constant energy contours, and the experimental QPI patterns of the two surfaces of WTe_2.

[32] W. Zhang, Q. Wu, L. Zhang, S. W. Cheong, A. A. Soluyanov, and W. Wu, Phys. Rev. B **96**, 165125 (2017).

[33] C. L. Lin, R. Arafune, R. Y. Liu, M. Yoshimura, B. J. Feng, K. Kawahara, Z. Y. Ni, E. Minamitani, S. Watanabe, Y. G. Shi, M. Kawai, T. C. Chiang, I. Matsuda, and N. Takagi, ACS Nano **11**, 11459 (2017).

[34] Y. S. Fu, T. Hanaguri, K. Igarashi, M. Kawamura, M. S. Bahramy, and T. Sasagawa, Nat. Commun. **7**, 10829 (2016).

[35] G. Kresse and J. Furthmüller, Phys. Rev. B **54**, 11169 (1996).

[36] P. E. Blöchl, Phys. Rev. B **50**, 17953 (1994).

[37] J. P. Perdew, K. Burke, and M. Ernzerhof, Phys. Rev. Lett. **77**, 3865 (1996).

[38] S. Kourtis, J. Li, Z. Wang, A. Yazdani, and B. A. Bernevig, Phys. Rev. B **93**, 041109(R) (2016).

[39] L. Peng, Y. Yuan, G. Li, X. Yang, J. J. Xian, C. J. Yi, Y. G. Shi, and Y. S. Fu, Nat. Commun. **8**, 659 (2017).